Applying a mapped pseudospectral time-domain method in simulating diffractive optical elements

Xiang Gao

Department of Electrical and Computer Engineering, University of Delaware, Newark, Delaware 19716

Mark S. Mirotznik

Department of Electrical Engineering and Computer Science, The Catholic University of America, Washington, D.C. 20064

Shouyuan Shi and Dennis W. Prather

Department of Electrical and Computer Engineering, University of Delaware, Newark, Delaware 19716

Received July 24, 2003; revised manuscript received January 6, 2004; accepted January 12, 2004

A new technique for the analysis of two-dimensional diffractive optical elements, by use of the pseudospectral time-domain (PSTD) method, is presented. In particular, the method uses a nonuniform (NU) grid and a mapping technique to obtain very accurate spatial derivatives in an efficient manner. To this end, we present the formulation of the PSTD method by using a NU grid and compare its application to the analysis with that of the finite-difference time-domain (FDTD) method. Using only a fraction of the memory and a fraction of the computation time used by FDTD, the mapped PSTD was able to obtain very close results to FDTD. © 2004 Optical Society of America

OCIS codes: 350.3950, 050.1970, 220.3620.

1. INTRODUCTION

Pseudospectral methods have been developed since the 1970s to solve partial differential equations.[1,2] Unlike finite-difference algorithms, pseudospectral methods can obtain the spatial derivatives of smooth functions with exponential accuracy even with sampling as low as the Nyquist rate. Later, pseudospectral time-domain (PSTD) algorithms were introduced and applied to the solution of Maxwell's equations.[3–7] Depending on the basis functions used, there are two types of PSTD: One can be dubbed as Fourier PSTD, which uses a Fourier series and in so doing encompasses a periodic domain, and the other uses polynomials such as Chebyshev polynomials defined in a nonperiodic closed region. Because the second method is usually used in a multidomain fashion, it is sometimes referred to as multidomain PSTD in the literature.[8,9] For the multidomain PSTD, which uses the Chebyshev collocation points and the fast Fourier transform (FFT), the required sampling rate is π grid points per minimum wavelength. In multidomain PSTD the domain separation is usually along material interfaces. In this paper we study a multilevel diffractive optical element (DOE), which has a staircase profile, and we focus on the Fourier PSTD method, which we will refer to as simply the PSTD method. In the PSTD method, the periodicity implication of the FFT creates a wraparound effect,[10] which can be effectively eliminated by placing Berenger's perfectly matched layer[11] at the outermost boundary.[12] There have been several applications with such an implementation of the PSTD method in the literature, including subsurface radar applications,[5,10] plasma waveguides,[8,13] radar cross sections of dielectric and perfect electric conductor cylinders,[14] and surface-relief DOE.[15]

Because PSTD requires much less memory at the expense of moderately increased computational complexity, it is advantageous to solve electrically large problems. For problems in which small electromagnetic structures are involved, a denser grid has to be employed; thus its advantages in memory savings are less significant. Furthermore, it has been recognized recently that, in dealing with material discontinuities, the Gibbs phenomenon arises owing to the discontinuity in the first-order derivatives for some field components.[16,17] It was suggested that nonuniform (NU) grids, which are suitable for problems in which both large and small features are present at different locations, may also help alleviate (not eliminate) the Gibbs phenomenon when a locally denser grid is placed at the material interface.[16]

In the NU PSTD algorithm,[9,16,18] one has to use a NU FFT.[19–22] Most of the NU FFT algorithms developed thus far apply a similar strategy: i.e., first interpolate the NU sampled data into a uniform grid and then apply the regular FFT. When going back to the real space, one has to interpolate the NU sampled data from a uniform grid. A more simplified approach, which applies a coordinate transformation (or mapping) in obtaining spatial derivatives, has been developed long time ago.[23,24] In

1084-7529/2004/050777-09$15.00

this paper we will revisit this approach and establish a general procedure to construct a mapping curve with exponentially convergent Fourier coefficients. Specifically, we developed a simple iterative algorithm by using an exponential low-pass filter and a spline function to find a smooth function while keeping the staircase error minimal. As an example application, we apply this technique to a two-dimensional (2D) DOE that contains both small and large features.

To a significant extent, small-scale DOEs have been studied with the finite-difference time-domain (FDTD) method.[25] Because FDTD requires a very dense grid (>20 grid per wavelength), it is not well suited for DOEs that are very large compared with a wavelength. And, the DOE geometry is very much NU, as it contains very small features in the higher-order zones and relatively large features in the central zones. For these reasons, it is ideally suited for the mapped PSTD method. In this paper we exploit the DOE geometry, create a 2D NU grid, apply the mapped PSTD algorithm, and then compare the results obtained with the FDTD results. We also apply a recently developed weighted total field–scattered field method[17] to introduce a windowed plane-wave soft source.

To this end, this paper is organized in two major parts. Section 2 explains the mapped FFT and procedures to obtain a good mapping curve. Section 3 applies the mapped FFT to study the diffraction of an eight-level DOE and presents comparisons with FDTD results.

2. MAPPED FAST FOURIER TRANSFORM

In the mapped FFT technique, an N-point NU grid $\{x_j\}$ is mapped into a uniform grid $\{u_j\}$, through an $x-u$ mapping curve. Then the spatial derivatives of a function F, which is sampled at $\{x_j\}$, are obtained through

$$\left.\frac{\partial F}{\partial x}\right|_{x=x_j} = \left.\frac{\mathrm{d}u}{\mathrm{d}x}\right|_{x=x_j} \left.\frac{\partial F}{\partial u}\right|_{u=u_j} = \left.\frac{\mathrm{d}u}{\mathrm{d}x}\right|_{x=x_j} \mathrm{IFFT}[ik\ \mathrm{FFT}(F)]|_{u=u_j}, \quad (1)$$

where $\mathrm{d}u/\mathrm{d}x$ is calculated only once for the entire simulation; IFFT is the inverse fast Fourier transform. In this case the mapping method is almost as efficient as the regular FFT algorithm, with a computation complexity of $O(N \log_2 N)$. Because the FFT algorithm is applied directly on the NU grid, any irregularity in the NU grid can produce an additional Gibbs phenomenon and thus make the calculation less accurate. In other words, the mapping curve should be as smooth as possible.

In general, to set up the $x-u$ curve, one can determine a subset of points on the $x-u$ curve directly from the real-space characteristic geometries, such as material boundaries. Our goal is to construct an analytically or exponentially smooth curve from those initial points, without introducing any staircase errors. To that end, we first use a commonly used spline function to construct a relatively smooth curve as an initial mold and then transform this curve into an exponentially convergent one by using an exponential low-pass filter. Because of the exponential convergence property of the resulting mapping curve, the derivatives can be obtained accurately with the FFT–IFFT technique. But applying such a filter will change the final shape of the mapping curve, result in grid positions shifted from original material interfaces, and create staircase errors. To address that problem, we developed a constraining technique to set up the initial polynomial curve.

A. Algorithm

For any $x-u$ mapping curve, as shown in Fig. 1(a), we introduce $\bar{x}_j$, which is the uniform grid position, as

$$\bar{x}_j = (x_{N+1} - x_1)\frac{j-1}{N} + x_1. \quad (2)$$

We also introduce x_j^*, which is the deviation of the NU grid to its corresponding uniform grid position and is shown in Fig. 1(b), as

$$x_j^* = x_j - \bar{x}_j. \quad (3)$$

Then we can represent x_j^* with a Fourier series:

$$x_n^* = \sum_{m=1}^{N} a_m \exp(ik_m u_n). \quad (4)$$

With the definitions of $\bar{x}_j$ and x_j^*, $\mathrm{d}x/\mathrm{d}u$ can be obtained as

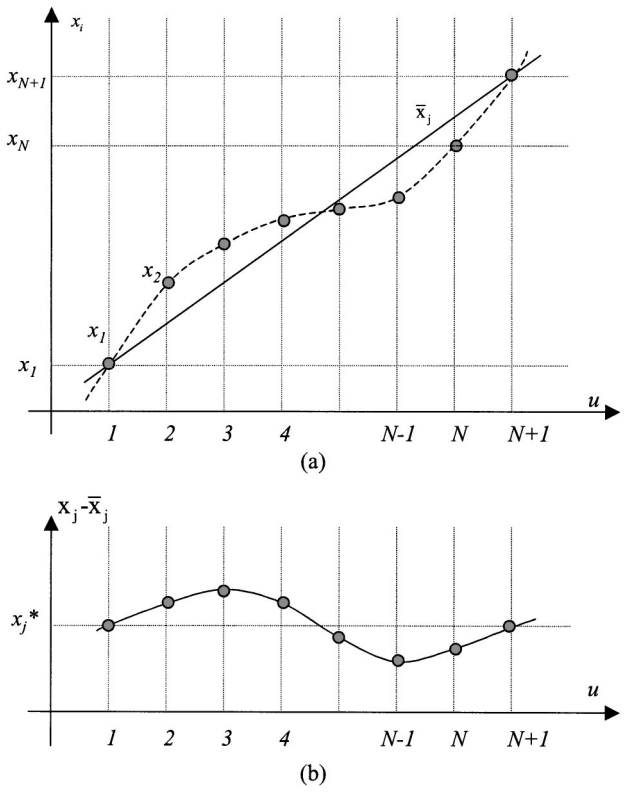

Fig. 1. Diagrams of (a) the $x-u$ points and the average position and (b) grid-position deviation x^*.

$$\left.\frac{\mathrm{d}x}{\mathrm{d}u}\right|_{u=j} = \left.\frac{\mathrm{d}(\bar{x} + x^*)}{\mathrm{d}u}\right|_{u=j} = \frac{x_{N+1} - x_1}{N} + \left.\frac{\mathrm{d}x^*}{\mathrm{d}u}\right|_{u=j}$$

$$= \frac{x_{N+1} - x_1}{N} + \mathrm{IFFT}[ik\ \mathrm{FFT}(x^*)]|_{u=j}. \quad (5)$$

In this case, $\mathrm{d}u/\mathrm{d}x$ is simply the inverse of $\mathrm{d}x/\mathrm{d}u$. From Eq. (5) we can see that to evaluate $\mathrm{d}u/\mathrm{d}x$ accurately x^* has to be suitable for the FFT–IFFT technique. That is to say, x^* has to be smooth. In general, one can always construct a well-behaved smooth function from polynomial interpolations, such as Lagrange interpolation and spline functions. But x^* values obtained from such polynomials tend to have a large flat tail for the high-order discrete Fourier transform coefficients.[2] Consequently, applying the FFT–IFFT technique directly cannot offer very accurate results. The simplest solution is to apply a narrow exponential low-pass filter to x^*, but our numerical experiments show that such filters have a direct impact on the resulting x^* values. If exact material boundary locations are included in the initial x^* values, then applying a filter can introduce staircase error. In applications where object geometry is curved or is so complicated that staircase error is unavoidable, this might not be a problem. But for the multilevel DOE profile studied in this paper, all interfaces are aligned along the main axes, so staircase error could be avoided. To minimize staircase error, we propose a simple constraining technique to find the initial polynomial fitted curve, which produces minimal staircase error when a low-pass filter is applied.

To see this, consider a subset of x^* values, $\{x_B^{*,0}\}$ given at subset $\{u_B\}$, where there are B such initial points and most are obtained from material interface information. From $\{x_B^{*,0}\}$ and $\{u_B\}$, one can use polynomial interpolation techniques to interpolate all x_l^* values at all u_l points. After application of an exponential low-pass filter on the interpolated complete set $\{x_l^{*,n}\}$, a new set $\{\underline{x}_l^{*,n}\}$ of $\underline{x}^*$ (underscore indicates filtered values) values is obtained. On the basis of the staircase errors $(\underline{x}_B^{*,n} - x_B^{*,0})$ at subset $\{u_B\}$, we adjust the corresponding $\{x_B^{*,n+1}\}$ values by using the following formula:

$$x_B^{*,n+1} = x_B^{*,n} - a(\underline{x}_B^{*,n} - x_B^{*,0}), \quad (6)$$

where the superscript n indicates the iteration number and constant a is usually chosen as 1. Repeat the above processes (interpolation, filtering, and staircase error evaluation, etc.) on the new set $\{x_B^{*,n+1}\}$ until the staircase error has the minimal value. This iteration algorithm is very robust and is less than 20 lines in our MATLAB program. As our numerical experiments show, this algorithm converges very fast, provided that the filter is not extremely narrow. We call this algorithm the constrained low-pass filtering (CLPF) technique.

B. Numerical Results of the Mapped Fast Fourier Transform

Figures 2 and 3 show the results of applying CLPF to two mapping curves. The dots in Figs. 2(a) and 3(a) are the initial points obtained from the object geometry, which will be explained in more detail in Section 3. From those initial points and the exponential low-pass filters shown in Figs. 2(b) and 3(b), we applied the CLPF technique to obtain the constrained spline function curves, which are indicated as dashed curves in Figs. 2(a) and 3(a). Because spline functions use finite-order polynomials to interpolate values, the spectrum for the constrained polynomial curves shows a large flat tail for the high-frequency coefficients as shown in Figs. 2(b) and 3(b). Then those two polynomial curves are smoothed with the exponential low-pass filter. The resulting mapping curves are very close to the initial points, and their spectrums are shown in Figs. 2(b) and 3(b), which clearly bear the exponential characteristics.[2] The flat plateau for high-frequency components is due to the machine-precision limit. Then the derivative $\mathrm{d}u/\mathrm{d}x$ and $\mathrm{d}u/\mathrm{d}y$ can be obtained through Eq. (5).

Figure 4 shows the convergence property of the CLPF technique. As can be seen, it takes only fewer than 100 iteration steps to obtain the minimal staircase error for the two mapping curves shown in Figs. 2(a) and 3(a).

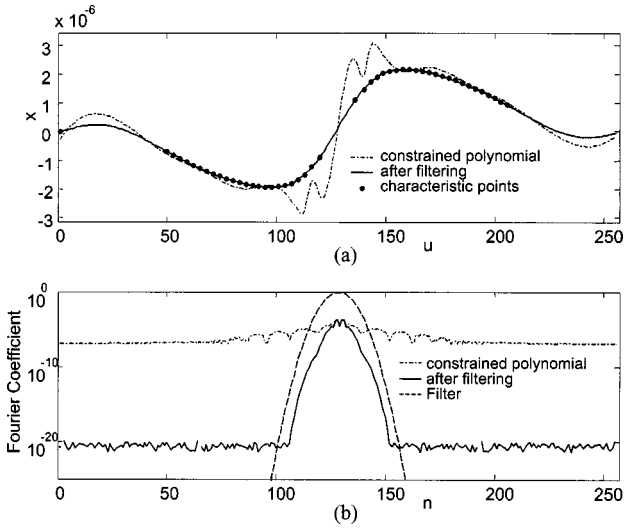

Fig. 2. Applying the CLPF technique to the x^*-u mapping curve. The resulting NU index is $\max(\Delta x)/\min(\Delta x) = 3.2298$.

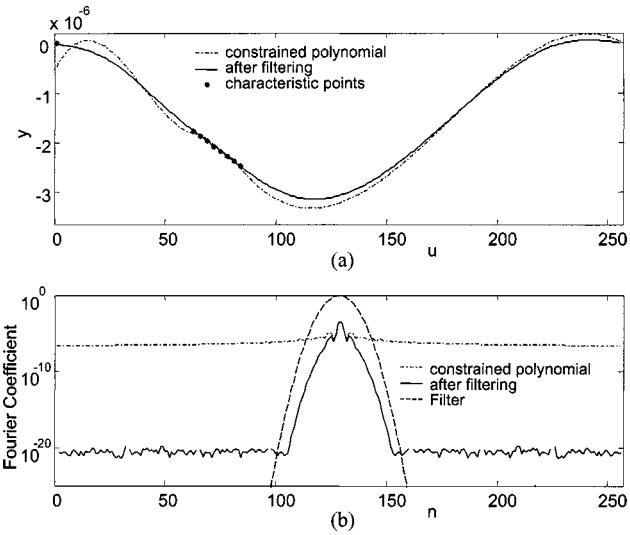

Fig. 3. Applying the CLPF technique to the y^*-u mapping curve. The resulting NU index is $\max(\Delta y)/\min(\Delta y) = 2.0754$.

Figure 5 also demonstrates the effectiveness of the CLPF technique; as can be seen, the staircase error is much smaller with CLPF.

Using the two mapping curves shown in Figs. 2(a) and 3(a), we further studied the accuracy in the derivative calculations for sinusoidal wave functions F with different wavelengths while keeping the total number of grid points fixed at 256. Figure 6 shows the errors in derivatives with and without applying the CLPF technique. Derivatives du/dx and du/dy are calculated with Eq. (5), and dF/du are calculated with the FFT–IFFT technique. Then dF/dx and dF/dy are obtained from Eq. (1). As can be seen, applying CLPF to the x^*-u and y^*-u curves can dramatically reduce the errors. Actually, it can achieve machine-limited accuracy at a high enough sampling rate. We believe that the spectral characteristics of the mapping curves x^*-u and y^*-u are the key to achieve such accuracy. There are many techniques to get a mapping curve with exponentially convergent Fourier coefficients. No matter what method is used, the high-frequency components should be as small as possible. In Fig. 6 the y^*-u curve is much more accurate than the x^*-u curve at a low sampling rate; we believe that this is due to the smaller NU index of the y^*-u curve.

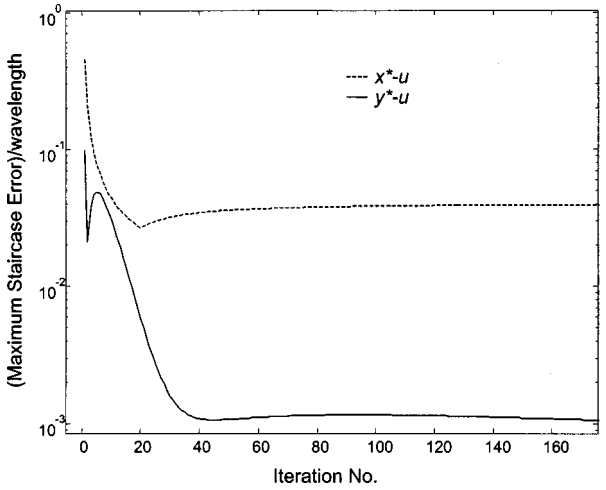

Fig. 4. Convergence of the CLPF technique. The two curves are the resulting staircase errors from the x^*-u and y^*-u curves shown in Figs. 2(a) and 3(a) while an iterative algorithm was used to reduce them. The wavelength shown on the y axis equals 1×10^{-6} and is used to normalize staircase errors.

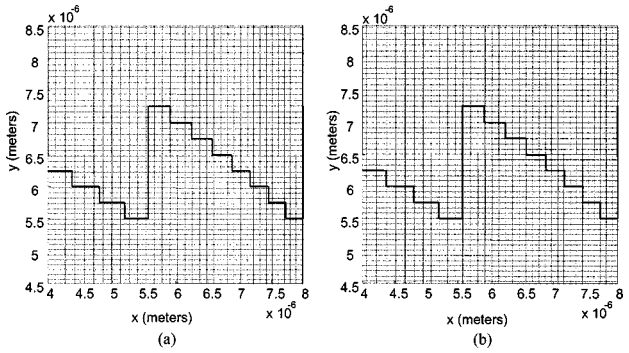

Fig. 5. (a) Close-up view of the NU grid obtained from the spline function and a low-pass filter without use of the constraining technique. (b) Close-up view of the NU grid obtained from the same filter function but with the CLPF technique applied. As can be seen, (a) shows visible staircase error, whereas in (b) the staircase error is much smaller.

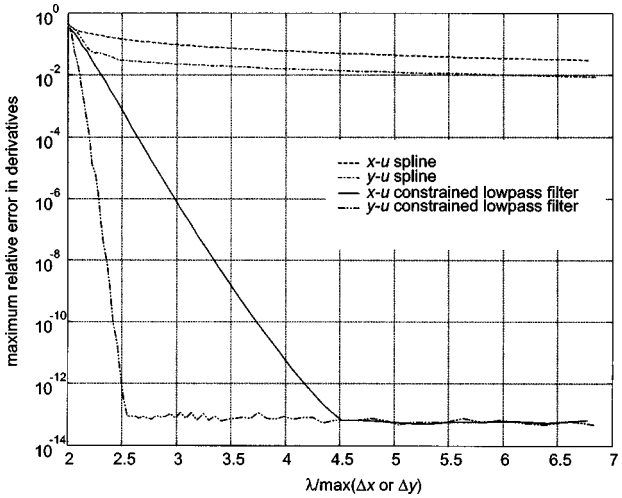

Fig. 6. Maximum relative errors in derivative calculations for the x^*-u and y^*-u curves shown in Figs. 2 and 3. Derivatives du/dx and du/dy are calculated with Eq. (5); dF/du are calculated with the FFT–IFFT technique. Machine-limited accuracy at a high sampling rate is achieved for the x^*-u and y^*-u curves when both are filtered. Without filtering, the errors are quite large.

3. APPLYING MAPPED PSEUDOSPECTRAL TIME DOMAIN ON THE SCATTERING OF A TWO-DIMENSIONAL DIFFRACTIVE OPTICAL ELEMENT

To study the scattering of a 2D DOE, we apply the mapped PSTD algorithm and mapped FFT algorithm described in Section 2. A diagram of the proposed NU grid and a DOE profile are shown in Fig. 7. We first set up the mapping curves for the x and y coordinates and then evaluate their error properties (see Fig. 6). The du/dx and du/dy values are then calculated before time marching and are stored for the entire simulation.

A. Diffractive Optical Element Structure, x^*-u and y^*-u Mapping Curves

Assuming that the DOE has a refractive index of n and a focal length of f, a continuous surface profile can be obtained from the following formula[26]:

$$h(x) = \mathrm{mod}\left[H_0 - \frac{1}{(n - n_0)}(\sqrt{x^2 + f^2} - f),\ H_0\right], \tag{7}$$

where $H_0 = \lambda_0/(n - n_0)$ provides a phase difference of 2π for neighboring zones. One approach of fabricating such small-scale DOEs is to use standard microfabrication techniques used in the integrated circuit industry. In general, a multilevel profile is used to approximate the continuous profile given in Eq. (7). As shown in Fig. 8, the continuous profile $h(x)$ can then be discretized into N uniform levels, where $h(x)$ is sampled at $h_m = -m\Delta h$

$= -m(H_0/N)$, with $m = 1, 2, \ldots, N$. For h_m, the corresponding x values can be obtained from Eq. (7) in a closed form.

In this case, x_m and h_m represent the characteristic points on the DOE profile. Note that there are multiple x values for a single h_m. For the sake of simplicity in notation, we indicate those characteristic points as (x_m, h_m) anyway, and they offer the basis for the NU grid in the x and y directions.

In our example application of the mapped PSTD, the DOE has eight levels, with fives zones and 47 small steps. The steps correspond to the short flat regions that have a phase shift of $2\pi/N$. Zones are the groups of neighboring steps that extend the full depth of the DOE profile and have a phase shift of 2π. The material is glass with a refractive index of 1.5 and is assumed to be semi-infinite. The incident wavelength is 1 μm, and the focal length is 15 μm. The DOE has an aperture of ~20 μm. Next, we explain the procedures to set up the x^*-u mapping curve in the x direction.

To construct the x^*-u curve with the x_m values, we must specify the number of grid points used between neighboring x_m values. This can be done with a simple interpolation program. To achieve a smooth and valid mapping curve, we impose some rules on inserting the sample points:

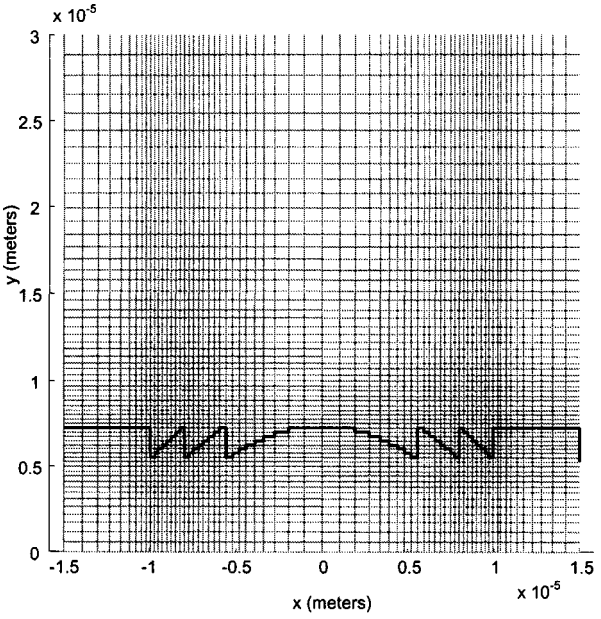

Fig. 7. Diagram of a 2D NU grid and a DOE profile.

1. For each step, there are at least R sample points. (R is a nonzero integer, and R can be specified initially.)
2. For all the neighboring steps in the DOE profile, the difference in the number of grid points should be kept as small as possible.
3. The maximum Δx should be smaller than $\lambda_{\min}/2$.

When the number of sampling points inserted between each x_m is determined, the x^*-u curve is uniquely specified. At this point we can utilize the CLPF technique described in Section 2 to further smooth out and obtain du/dx with Eq. (5). These procedures, including insertion of sampling points, constructing the x^*-u curve, and utilizing CLPF, are performed with computer programs. Similarly, the same procedures can be performed for the y axis from h_m. The results are given in Section 2. It should be pointed out that all those overhead calculations take less than a few seconds on an ordinary personal computer with a 400-MHz Intel processor.

B. Weighted Total-Field–Scattered-Field Pseudospectral Time Domain and Windowed Plane-Wave Generation

To introduce a windowed soft source for the DOE specified in Subsection 3.A with a mapped PSTD algorithm, we apply a weighted total-field–scattered-field method.[17] In that technique, weighted field components E and H are used, and the total field and scattered field regions are connected with a connecting region, where the incident soft source is introduced. We use the same field-splitting technique in Ref. 17 but add the incident fields on only one side of the connecting region (see Fig. 9). In this way we can create an internal windowed soft source.

Reference 17 introduces a weight scalar ζ, weighted field components $\hat{\mathbf{E}}_{\text{tot}}$, $\hat{\mathbf{H}}_{\text{tot}}$, and weighted incident field components $\hat{\mathbf{E}}_{\text{inc}}$ and $\hat{\mathbf{H}}_{\text{inc}}$:

$$\hat{\mathbf{E}}_{\text{tot}} = \hat{\mathbf{E}}_{\text{inc}} + \mathbf{E}_{\text{scat}} = \zeta \mathbf{E}_{\text{inc}} + \mathbf{E}_{\text{scat}},$$

$$\hat{\mathbf{H}}_{\text{tot}} = \hat{\mathbf{H}}_{\text{inc}} + \mathbf{H}_{\text{scat}} = \zeta \mathbf{H}_{\text{inc}} + \mathbf{H}_{\text{scat}}. \quad (8)$$

ζ is chosen to be 0 in the SF zone and 1 in the total field zone and to continuously change from 0 to 1 in the connecting region.

We use the split-field perfect-matching-layer equations for the 2D TE_z mode scattering. After using the transform $H_{\text{new}} = Z_0 H_{\text{old}} = (\mu_0/\epsilon_0)^{1/2} H_{\text{old}}$ and some derivations from the split-field perfect-matching-layer equations, we obtain the following equations for the weighted $\hat{\mathbf{E}}$ and $\hat{\mathbf{H}}$ fields:

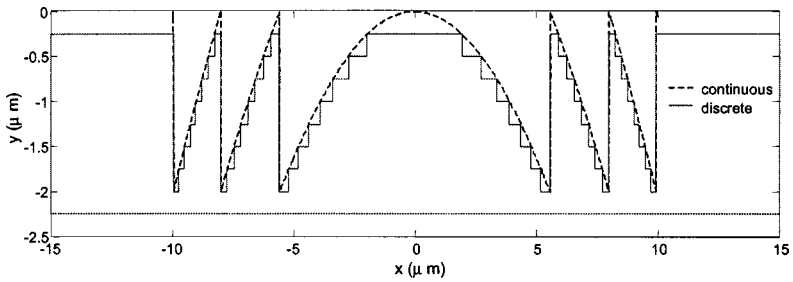

Fig. 8. Diagram of the discretization of a multilevel DOE. The location of the characteristic points (x_m, h_m), where the discretized profile coincides with the continuous one, uniquely determines the geometry of the discretized profile.

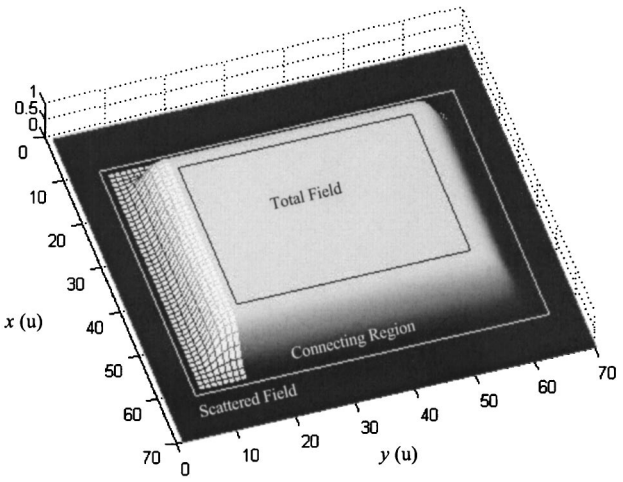

Fig. 9. Diagram of weight function ζ. The region where $\zeta = 1$ is the total field, and $\zeta = 0$ corresponds to the scattered field. The connecting region is where ζ is between 0 and 1. The incident terms should be added to all the connecting regions. But if the incident wave is added only to the meshed region shown in this figure, a windowed soft source can be created for the region above the meshed region.

$$\frac{\partial \hat{E}_x}{\partial t} = \frac{c}{\epsilon_r}\left(\frac{\partial \hat{H}_z}{\partial y} - \frac{\partial \zeta}{\partial y} H_{z\_\mathrm{inc}}\right) - \frac{\sigma_y}{\epsilon_r \epsilon_0}\hat{E}_x,$$

$$\frac{\partial \hat{E}_y}{\partial t} = -\frac{c}{\epsilon_r}\left(\frac{\partial \hat{H}_z}{\partial x} - \frac{\partial \zeta}{\partial x} H_{z\_\mathrm{inc}}\right) - \frac{\sigma_x}{\epsilon_r \epsilon_0}\hat{E}_y,$$

$$\frac{\partial \hat{H}_{zx}}{\partial t} = -\frac{c}{\mu_r}\left(\frac{\partial \hat{E}_y}{\partial x} - \frac{\partial \zeta}{\partial x} E_{y\_\mathrm{inc}}\right) - \frac{\sigma_x^*}{\mu_r \mu_0}\hat{H}_{zx},$$

$$\frac{\partial \hat{H}_{zy}}{\partial t} = \frac{c}{\mu_r}\left(\frac{\partial \hat{E}_x}{\partial y} - \frac{\partial \zeta}{\partial y} E_{x\_\mathrm{inc}}\right) - \frac{\sigma_y^*}{\mu_r \mu_0}\hat{H}_{zy}, \tag{9}$$

where $\hat{H}_z = \hat{H}_{zx} + \hat{H}_{zy}$ and $\hat{S} = \zeta S_{\mathrm{inc}} + S_{\mathrm{scat}}$. S represents the E and H components.

In general, the scattered field and total field can be arranged as shown in Fig. 9, but we add incident terms only at the meshed region in Fig. 9. This is very efficient to implement, since most of the additional incident terms in Eqs. (9) are simply zero. The region above the meshed region in Fig. 9 becomes the total field in effect. The shape of the window function is obtained from an integral form of the Blackman–Harris window function.[17] This is slightly different in shape from the soft source we used in the FDTD comparison, which is, instead, a raised cosine. Because the total width of the window is much larger than the edge width, the difference in incident field is minimal.

The geometry of the windowed soft source we used in our mapped PSTD calculation is as follows. It has a total width of 20.28 μm, including two smoothing edges of 0.95 μm at each side. The closest distance from the soft source to the DOE surface, which is also the distance from the lower edge of the total field region to the DOE surface, is 5.15 μm. The height of the soft-source region, which is also the height for the meshed connecting region shown in Fig. 9, is 1.22 μm.

C. Numerical Results

We tested our mapped PSTD algorithm for a 2D TE_z mode scattering of the 2D DOE specified in Subsection 3.A. The size of the computation region is $L_x \times L_y = 30\,\mu\mathrm{m} \times 30\,\mu\mathrm{m}$. We also compared the results with those obtained with the FDTD method. The FDTD computation is carried out with a sampling rate of 40 grids per wavelength ($\Delta x = \Delta y = 0.025\,\mu$m) to minimize numerical dispersion and staircase errors. In total, there are 1.44×10^6 grid points for the FDTD calculation. The mapped PSTD, on the other hand, uses 65.6×10^3 grid points, or 1/22 the memory usage in FDTD. The steady state is reached after the incident wave has traveled approximately 120 μm, which requires 4780 and 9560 time steps for the mapped PSTD and FDTD we used, respectively. We run the simulations on a personal computer with 2-GB memory and one 2-GHz CPU. It takes 14 min to finish for the mapped PSTD and 157 min for FDTD. The steady-state results from the FDTD algorithm are then mapped into the NU grid used by the mapped PSTD, with a linear interpolation. The results are then compared with the mapped PSTD, shown in Figs. 10–12. As can be seen in Figs. 11 and 12, the differences are very small. For all the field components, the difference is around -20 dB in most regions.

Because far fewer grid points are used in the mapped PSTD, it actually runs faster than FDTD despite the fact that additional FFT operations are needed. A general discussion of the computational complexity of PSTD and FDTD can be found in Ref. 5. It was pointed out[5] that, at each time step, the ratio of CPU time required by FDTD and PSTD is $F = 2K_1 \times (M_{\mathrm{FD}}/M_{\mathrm{PS}})^D/K_2 \log_2 M_{\mathrm{PS}}$, where M_{FD} and M_{PS} are the number of grid points in each dimension for FDTD and PSTD, respectively, and K_1 and K_2 are constants associated with the characteristic computing speed in FDTD and PSTD respectively. In our case, $F = 7.925K_1/K_2$. And our numerical experiments show $F \cong (157/9560)/(14/4780) = 5.61$, yielding $K_1/K_2 \cong 0.71$. The performance comparison of the mapped PSTD and FDTD is also given in Table 1.

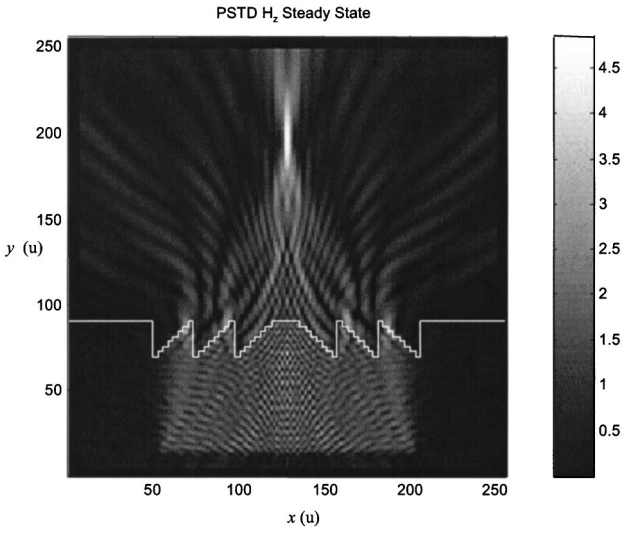

Fig. 10. Steady-state result of $|H_z|$ obtained from the mapped PSTD algorithm. The image is on a NU rectangular grid.

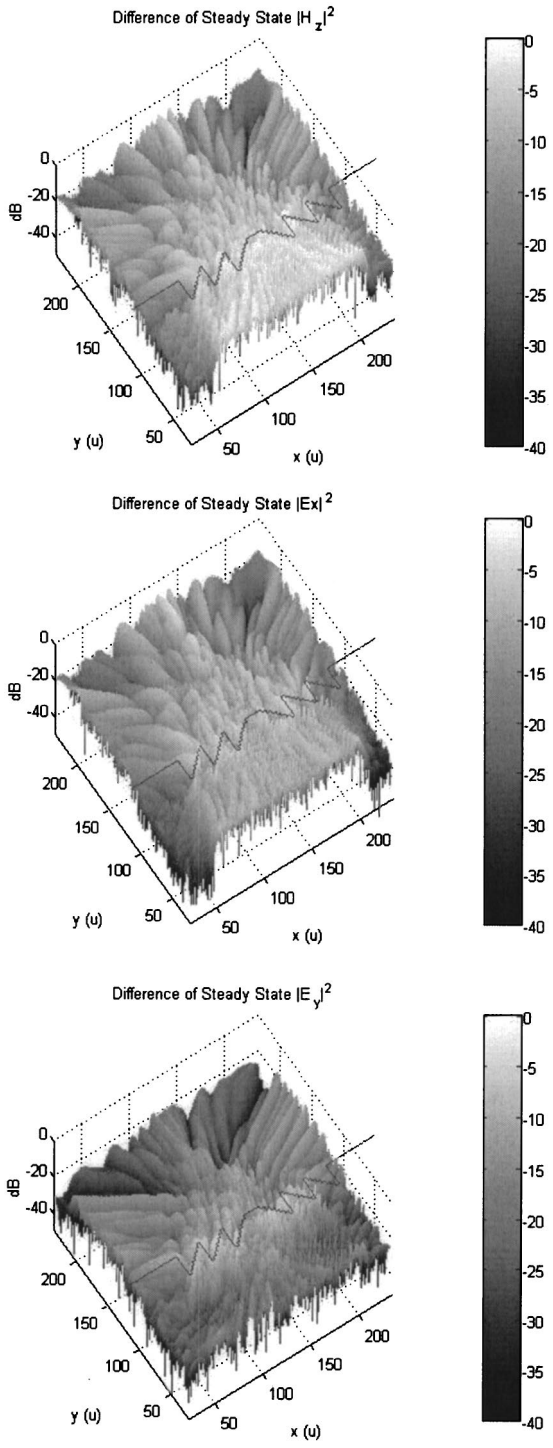

Fig. 11. Absolute difference of $|H_z|^2$, $|E_x|^2$, and $|E_y|^2$ steady-state values from FDTD and the mapped PSTD. x and y coordinates are grid numbers. The scattered field region in the mapped PSTD is excluded. The DOE profile is also plotted.

4. DISCUSSION

To set up the NU grid, we use the characteristic points on the DOE to construct a mapping curve, from which the exact grid positions are then interpolated. If we apply an exponential low-pass filter directly to smooth the mapping curve, the resulting grid points are shifted slightly away from the exact boundary. We can define this offset as the staircase error. Without constraining the polynomial curve and applying a low-pass filter directly, we find that the average staircase error is 0.137 MFx [minimum feature (MF)] for the x grid and 0.06 MFy for the y grid, where MFx = 0.228 μm and MFy = 0.250 μm are the minimum feature size in the x and y directions, respectively. Those staircase errors are equivalent only to a uniform grid of roughly 250 grid points in the x direction and 500 grid points in the y direction. When the constraining technique was applied, the staircase error was reduced to 0.0319 MFx and 0.0023 MFy for the x and y grids, respectively. If a uniform grid should be used to match these staircase errors, it would need more than 1030 grid points in the x direction and more than 13,000 grid points in the y direction! Clearly, in this case using a NU grid and carefully aligning grid points with material interfaces is significantly more advantageous than using a uniform grid. In fact, for the DOE profile studied, unless a NU grid is used, a regular PSTD algorithm cannot offer any computational advantage, owing to the requirement of a grid density close to FDTD. However, the mapped PSTD in this paper can offer a memory savings of 22 and a computation time savings larger than 10.

Also, because a much larger grid spacing is used for the mapped PSTD, the time step can be larger than that used for FDTD (see Table 1). We use the stability requirements for uniform PSTD to estimate the upper limit of dt. However, we found with our numerical experiments that this requirement is too stringent for the mapped PSTD. In fact, a slightly larger dt can used. We believe the du/dx and du/dy terms in the mapped PSTD cause the stability requirement to be slightly relaxed.

One particular issue is the Gibbs phenomenon, which arises when PSTD is applied to materials with discontinuous properties. Assume a function F is to be represented by a Fourier series and F is associated with 0 to N–1-order derivatives. If the kth (and higher) derivative is discontinuous, then it is said to have a jump of order k. The error due to the Gibbs phenomenon at the jump location is $O(N^{-k})$ and $O(N^{-k-1})$ for locations some distance away from the jump. When perfectly conducting materials are dealt with, the jumps in some field values at the material interface are of the 0th order. That is the reason that PSTD is not applied to those materials. For dielectric materials, assuming all interfaces are aligned to one of the x, y, or z axes, the tangential field components (which need to take derivatives along their vertical directions) are continuous; thus, even when materials are discontinuous, the error introduced is $O(N^{-2})$ for locations away from the jump. Using a locally denser grid can reduce the magnitude of the jump of the 1st-order derivatives in a uniform grid. Specifically this 1st-order jump (dF/du) is the 1st-order jump in real space (dF/dx) scaled by the dx/du value at the jump location, where a locally denser grid can yield very small dx/du. Thus it can reduce the effect of the Gibbs phenomenon. Nevertheless, the Gibbs phenomenon is a serious issue and should be addressed for the PSTD algorithm, i.e., if the PSTD is applied to high-contrast or perfectly conducting materials. In this paper, to reduce the Gibbs phenomenon, we also use the average material property for grid points located on the DOE surface.

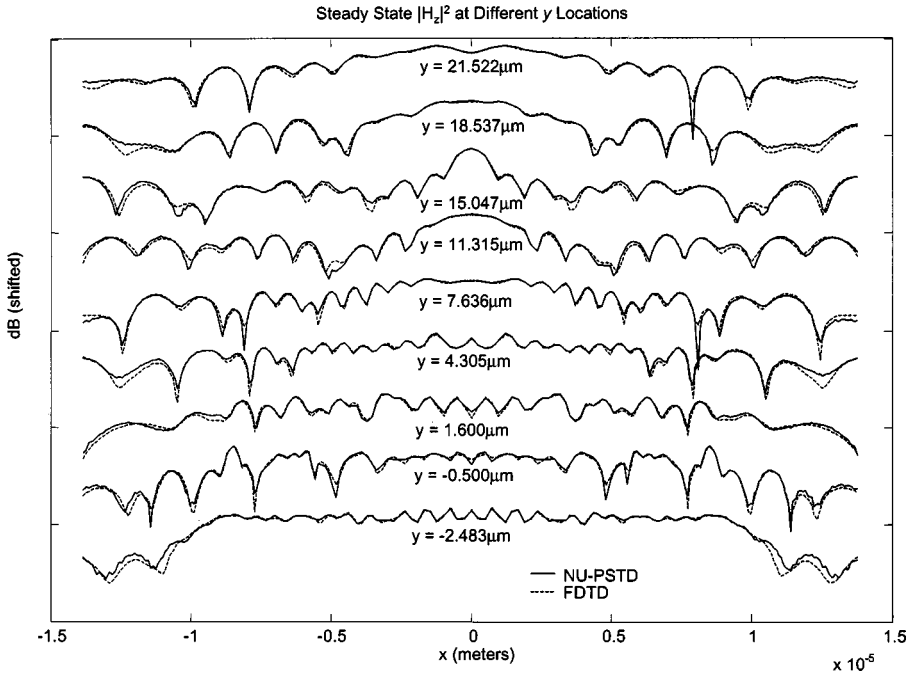

Fig. 12. x-direction line scan of steady-state $|H_z|^2$ at several distances away from the DOE surface. The locations are randomly picked. To avoid overlapping, curves at different locations are shifted differently. But curves at the same y location are shifted the same amount for the mapped PSTD and FDTD. Negative y's correspond to locations below the DOE surface.

Table 1. Performance Comparison of Mapped PSTD and FDTD

Method	Grid Size	Minimum Grid Spacing (μm)	Maximum dt from Stability Requirement (s)	dt Used in Computation (s)	Total Computing Time [stop at $t = 3.986091 \times 10^{-13}$ (s)] (min)
Mapped PSTD	256 × 256	0.0755	11.3220×10^{-17a}	8.3391×10^{-17}	14 (4780 time steps)
FDTD	1200 × 1200	0.0250	5.8925×10^{-17b}	4.1696×10^{-17}	157 (9560 time steps)

[a] Obtained from d$t < 0.4502\,$dx/c for 2D uniform PSTD[5]; however, for the mapped PSTD program, numerical experiments show that dt can be as large as 13.000×10^{-17} s in this case.

[b] Obtained from d$t < 0.7071\,$dx/c for 2D FDTD.[25]

5. CONCLUSION

We have applied the mapped PSTD algorithm to study 2D DOEs. To that end, we presented procedures to construct smooth mapping curves to map the nonuniform grid into a uniform one. To reduce the staircase error and smooth the mapping curve obtained from spline functions, we developed a simple constraining algorithm combined with an exponential low-pass filter. With this technique, the staircase error is greatly reduced. In the end, by use of a much smaller grid size, a NU grid can achieve a better representation of the DOE profile than a uniform grid. Also, because the mapping curve is effectively smoothed, very high accuracy in derivatives can be obtained from the spectral components of the mapping curve. Having verified the accuracy in derivative calculations and the accuracy in representing the DOE profile, we further applied the mapped PSTD algorithm to study the scattering of the DOE. To launch a windowed soft source, we also applied a recently developed new technique for PSTD. The steady state is achieved after the wave travels a long enough time. The same problem was also studied with FDTD, with a similar windowed soft source, which propagates for the same time period and is scattered by the same DOE profile. The results from FDTD and PSTD are compared and are shown to be very close.

The mapped PSTD algorithm presented can take advantage of both the PSTD algorithm, which requires much less memory than the finite-difference techniques, and a NU grid, which can represent a DOE structure more efficiently than a uniform grid. In summary, although far fewer grid points are used in our calculation (~1/22 of FDTD), we obtained results very close to the FDTD methods in less than one tenth of the computation time.

The success of the mapped PSTD algorithm relies on the fact that the DOE profile is relatively simple, so that carefully constructing a NU grid can yield a very small staircase error. For objects with very irregular profiles, such as subwavelength DOEs, it might be very difficult to

achieve minimal staircase errors while using far fewer grid points than a uniform grid uses. Apparently, more case studies are needed for different dielectric DOEs.

X. Gao, the corresponding author, can be reached by e-mail at xigao@ee.udel.edu.

REFERENCES

1. D. Gottlieb and S. A. Orszag, *Numerical Analysis of Spectral Methods: Theory and Applications* (Society for Industrial and Applied Mathematics, Philadelphia, Pa., 1977).
2. J. P. Boyd, *Chebyshev and Fourier Spectral Methods*, 2nd ed. (Dover, Mineola, New York, 2001).
3. A. V. Kabakian, "A spectral algorithm for electromagnetic wave scattering in the time domain application to RCS computation," in *Proceedings of the 27th AIAA Plasmadynamics and Lasers Conference* (American Institute of Aeronautics and Astronautics, www.aiaa.org, 1996), Paper 96-2334.
4. Q. H. Liu, "A spectral-domain method with perfectly matched layers for time-domain solutions of Maxwell's equations," presented at the 1996 URSI Meeting, Baltimore, Md., July 1996.
5. Q. H. Liu, "The PSTD algorithm: a time-domain method requiring only two cells per wavelength," Microwave Opt. Technol. Lett. **15**, 158–165 (1997).
6. B. Yang, D. Gottlieb, and J. S. Hesthaven, "On the use of PML ABC's in spectral time-domain simulations of electromagnetic scattering," in *Proceedings of the ACES 13th Annual Review of Progress in Applied Computational Electromagnetics* (Applied Computational Electromagnetics Society, http://aces.ee.olemiss.edu, 1997), pp. 926–933.
7. Y. F. Leung and C. H. Chan, "Pseudospectral time-domain (PSTD) method with unsplit-field PML," Microwave Opt. Technol. Lett. **22**, 278–283 (1999).
8. G. X. Fan and Q. H. Liu, "FDTD and PSTD simulations for plasma applications," IEEE Trans. Plasma Sci. **29**, 341–348 (2001).
9. B. Tian and Q. H. Liu, "Nonuniform fast cosine transform and Chebyshev PSTD algorithms," Prog. Electromagn. Res. **28**, 253–273 (2000).
10. Q. H. Liu, "Large-scale simulations of electromagnetic and acoustic measurements using the pseudospectral time-domain (PSTD) algorithm," IEEE Trans. Geosci. Remote Sens. **37**, 917–926 (1999).
11. J. P. Berenger, "A perfectly matched layer for the absorption of electromagnetic waves," J. Comput. Phys. **114**, 185–200 (1994).
12. Q. H. Liu, "PML and PSTD algorithm for arbitrary lossy anisotropic media," IEEE Microwave Guid. Wave Lett. **9**, 48–50 (1999).
13. Q. H. Liu, "A frequency-dependent PSTD algorithm for general dispersive media," IEEE Microwave Guid. Wave Lett. **9**, 51–53 (1999).
14. Q. L. Li, Y. C. Chen, and D. Ge, "Comparison study of the PSTD and FDTD methods for scattering analysis," Microwave Opt. Technol. Lett. **25**, 220–226 (2000).
15. J. S. Hesthaven, P. G. Dinesen, and J. P. Lynov, "Spectral collocation time-domain modeling of diffractive optical elements," J. Comput. Phys. **155**, 287–306 (1999).
16. Q. H. Liu, X. M. Xu, B. Tian, and Z. Q. Zhang, "Applications of nonuniform fast transform algorithms in numerical solutions of differential and integral equations," IEEE Trans. Geosci. Remote Sens. **38**, 1551–1560 (2000).
17. X. Gao, D. W. Prather, and M. S. Mirotznik, "A method for introducing soft sources in the PSTD algorithm," IEEE Trans. Antenna Propag. (to be published).
18. W. K. Leung and Y. C. Chen, "Transformed-spaced nonuniform pseudospectral time-domain algorithm," Microwave Opt. Technol. Lett. **28**, 391–396 (2001).
19. J. W. Cooley and J. W. Tukey, "Algorithm for the machine computation of complex Fourier series," Math. Comput. **19**, 297–301 (1965).
20. A. Dutt and V. Rokhlin, "Fast Fourier transforms for nonequi-spaced data," SIAM J. Sci. Comput. **14**, 1368–1393 (1993).
21. N. Nguyen and Q. H. Liu, "The regular Fourier matrices and non-uniform fast Fourier transforms," SIAM J. Sci. Comput. **21**, 283–293 (1999).
22. Q. H. Liu, "An accurate algorithm for nonuniform fast Fourier transforms," IEEE Microwave Guid. Wave Lett. **8**, 18–20 (1998).
23. C. Canuto, M. Y. Hussaini, A. Quarteroni, and T. A. Zang, *Spectral Methods in Fluid Dynamics* (Springer-Verlag, New York, 1987).
24. A. Bayliss and E. Turkel, "Mappings and accuracy for Chebyshev pseudo-spectral methods," J. Comput. Phys. **101**, 342–359 (1992).
25. A. Taflove and S. C. Hagness, *Computational Electrodynamics: the Finite-Difference Time-Domain Method*, 2nd ed. (Artech House, Norwood, Mass., 2000).
26. X. Gao, "Design, fabrication and characterization of small diffractive optical elements," M.S. thesis (University of Delaware, Newark, Delaware, 2000).